



LES study of near-seabed tide-induced turbulence in the East China Sea



Yoshinobu Wakata^{a,*}, Takahiro Endoh^b, Yutaka Yoshikawa^c

^a Research Institute for Applied Mechanics, Kyushu University, 6-1, Kasuga-Kohen, Kasuga, Fukuoka 816-8580, Japan

^b UTokyo Ocean Alliance, The University of Tokyo, Tokyo, Japan

^c Division of Earth and Planetary Sciences, Graduate School of Science, Kyoto University, Kyoto, Japan

ARTICLE INFO

Keywords:

Near-seabed turbulence
Large eddy simulation
East China Sea
Tides
Critical latitude
Turbulent dissipation rate

ABSTRACT

Near-seabed turbulent properties observed in the East China Sea were investigated using a large eddy simulation (LES) model. Tidal forcing estimated from the observed tidal current is imposed to the LES model assuming a flat seabed. Turbulence stirred by tidal currents near the seabed is simulated and compared to observed turbulence. The observed tide is dominated by the M_2 constituent. The energy dissipation rate evolves with a quarter-day period near the seabed, whereas the dissipation rate evolves with a diurnal period in the upper part of the boundary layer. Salinity also oscillates diurnally. Thickness of the boundary layer related to K_1 is thicker than that of M_2 . Orientation of the major axis of M_2 in the tidal ellipse does not change downward, but that of K_1 rotates counterclockwise. The vertical structure difference of two constituents is attributable to the observation site latitude, which is approximately the critical latitude of K_1 . All of these features are simulated in the LES model. Particularly, results show that the interference of M_2 and K_1 induces diurnal variation of the turbulent dissipation rate in the upper part of the boundary layer through the turbulent energy production rate controlled by the vertical shear. A hypothetical simulation without horizontal advection demonstrate that this process can contribute more to the diurnal variation in the upper part of the boundary layer than stratification stability control owing to salinity advection through tidal straining.

1. Introduction

Continental shelf seas are the main areas in which tidal energy is dissipated. Turbulence induced by tides in shallow seas can transport vast amounts of nutrients from nearby seabed areas to the photic layer. For that reason, continental seas account for a large share of oceanic primary production (Furevik and Foldvik, 1996) and play an important role in CO_2 storage (Thomas et al., 2004). Furthermore, through bottom friction and vertical density mixing, turbulence can affect large-scale circulation. Understanding the turbulence that occurs in continental shelf seas is therefore an important topic.

Recently, the energy dissipation rate, representing the turbulence property, can be observed using a turbulence structure profiler. However, to elucidate turbulence related to forcing comprehensively, synchronous information related to background fields such as currents, temperature, and salinity is also needed. Such integrated observations were conducted by Lueck and Lu (1997) and Lu et al. (2000) for the rectilinear flow passing the Cordova Channel between Vancouver Island and the North American mainland. Those observations clarify the logarithmic layer structure near the seabed. Furthermore, Simpson et al. (1996) observed the vertical structure of turbulent dissipation in

the Irish Sea using the free-fall FLY profiler. They found the dissipation rate for the upper part of the benthic boundary layer, forced by the strong shear near the seabed related to the tidal current. This dissipation rate repeatedly increased and decreased with a quarter-day period M_4 related to the M_2 tidal constituent. It has a phase delay of more than 4 h relative to that near the seabed.

Observational results can be simulated well using a vertical one dimensional model with the Mellor–Yamada turbulence model (Mellor and Yamada, 1974, 1982), except for areas above the thermocline. Burchard et al. (1998) further investigated turbulence properties after Simpson et al. (1996) using some vertically one dimensional ensemble closure models. They conducted comparative studies for some Mellor–Yamada models and a k - ϵ model. Their results demonstrate that the time delay of peaks for the dissipation rate is about 1 h relative to the current speed peak. Although these ensemble closure models are useful for simulating large-scale ocean circulation, they inevitably include some tunable parameters such as stability functions and representative barotropic length scale (Burchard et al., 1998), which are usually tuned so as to fit the observations. Additionally, they cannot reproduce small turbulent eddies, even when using a very fine grid size, because ensemble mean statistical results are used for estimating the model

* Corresponding author.

E-mail address: wakata@riam.kyushu-u.ac.jp (Y. Wakata).

parameters.

In contrast, a large eddy simulation (LES) model consists of a grid-scale model solving the turbulent large eddy and the sub-grid model related to the inertia subrange scale eddy. Namely, LES includes hypotheses less than the ensemble closure model depending on the stability function as discussed Basu et al. (2004). It is useful to solve the large turbulent eddy itself. The Reynolds stress and the eddy viscosity can be estimated directly from the resolved eddy components. Actually, LES was applied by McWilliams et al. (1997) and Skyllinstad (1999) to currents near the sea surface. Metais (1998) applied LES to geostrophic currents. Li et al. (2005, 2008, 2010) and Wakata (2010, 2011) applied LES to estuary circulation. From a theoretical perspective, several studies have examined turbulence for an oscillating flow in ideal situations.

Salon et al. (2007) and Gayen et al. (2010) analyzed the turbulence that develops under an oscillating flow in a frame without Earth rotation. Gayen et al. (2010) demonstrated that the turbulence development for acceleration and deceleration of flow velocity is asymmetric. Momen and Bou-Zeid (2016) investigated turbulence developed under unsteadily oscillating flow. Several LES studies have undertaken, however direct comparisons with observations that have not been accomplished well, especially for the continental shelf ocean, because the integrated observation data are necessary and the LES model is difficult to tune because of the absence of control parameters. For the ocean physics, LES is an very important tool. Perhaps only by examining the reproducibility of the observation can we assess the validity of LES and understand its shortcomings. We will touch this point.

Endoh et al. (2016) recently observed turbulence above the continental shelf in the East China Sea for periods of a few days. They observed currents, temperature, salinity, and the turbulent energy dissipation rate in the continental shelf of the East China Sea with 68 m depth (31°44.9'N, 125°50.0'E, Fig. 1) during 16–21 July, 2011. The dissipation rate varied on a temporal basis more actively than the results reported by Simpson et al. (1996). The observation site seabed, consisting of mud, is almost flat, inclined slightly east–northeastward. There are tidal currents with dominant semidiurnal constituent M_2 and small diurnal constituent K_1 . They do not indicate the constituents themselves but are, respectively, representative of the fluctuations with similar frequencies.

Endoh et al. (2016) found the appearance of unstable stratification with a half day period in the lower part of the bottom boundary layer, which was explained in terms of the “Shear-Induced Convection” (ShIC) mechanism (Lorke et al., 2005), which is attributable to upslope and downslope currents near the seabed caused by the rotation of the M_2 flow direction.

The turbulent energy dissipation rate varied with a quarter-day period near the seabed because the flow velocity related to M_2 has peaks four times a day, when the flow direction is oriented to the direction of the major axis of the tidal ellipse. This feature is commonly seen in near seabed turbulence that develops under the tidal current with a flattened tidal ellipse (Simpson et al., 1996). However, the dissipation rate varied with a diurnal period in the upper part of the bottom boundary. The cause of this variation was not clarified by Endoh et al. (2016). The main target of the present research is therefore to clarify this mechanism.

As described in this paper, we use the LES model to simulate the turbulent behavior related to the observed ocean field by Endoh et al. (2016). We particularly address the turbulent property in the upper part of the bottom boundary layer, i.e. energy dissipation rate, controlled by the vertical shear related to the tidal current and the horizontal density advection. It is noteworthy that neither upslope nor downslope current effects in ShIC are included because we assume a flat bottom.

The LES model is solved by imposing tidal forcing estimated from Acoustic Doppler Current Profiler (ADCP) current data. The dissipation

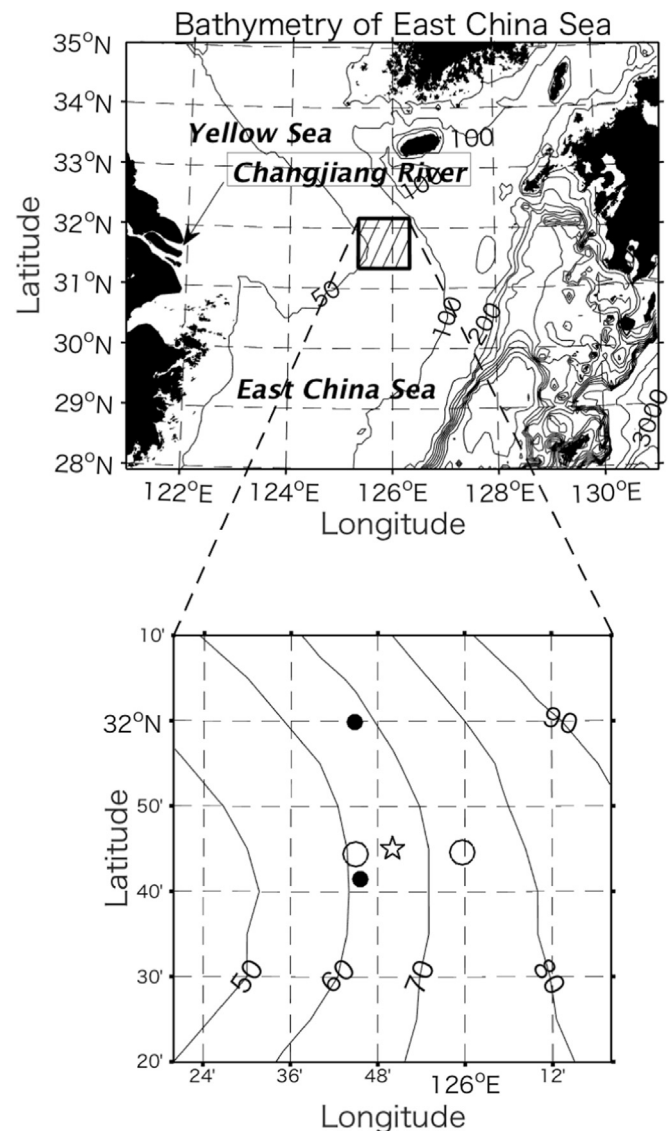


Fig. 1. Map of the East China Sea. Contours are bathymetric (m). Star symbols represent sites of ADCP and TurboMAP-5 (turbulence structure profiler) (Endoh et al., 2016). Circle symbols represent CTD stations.

rate from the sub-grid model is compared with the turbulence structure profiler observations. Furthermore, we specifically examine the mechanisms of their temporal variation.

2. Model configuration

We used a parallelized large-eddy simulation model (PALM), developed at Hannover University by Raasch and Schröter (2001) and Maronga et al. (2015), for LES numerical simulations. This model solves Navier–Stokes equations in Cartesian coordinates with Coriolis force and Boussinesq approximation. These governing equations are separated into a resolved grid scale (GS) and sub-grid-scale (SGS) using a local spatial filter. For the SGS model, turbulent energy was solved according to Deardorff (1980) with minor changes. The computational domain was $200 \times 200 \times 66$ m. The periodic boundary condition was assumed for horizontal direction. The depth was set to 66 m, corresponding to the ocean depth at the observation point. The top boundary condition of velocity was slip. The heat and salinity flux at the sea surface were zero. The bottom boundary was flat and motionless. A Prandtl boundary layer was assumed between the seabed and the first computational grid level as representing the no-slip

condition. The bottom roughness height was 0.0001 m, representing the muddy seabed. The sensitivity for this parameter was not so high. The grid size was $0.5 \times 0.5 \times 0.26$ m. The model latitude was set as 31.75°N .

The GS momentum equations are described here; variables shown with a bar are GS variables.

$$\frac{\partial \bar{u}_i}{\partial t} = -\frac{\partial \bar{u}_j \bar{u}_i}{\partial x_j} - \frac{1}{\rho_0} \frac{\partial \bar{\pi}^*}{\partial x_i} - \varepsilon_{ijk} f_j \bar{u}_k - g \frac{\bar{\rho} - \rho_0}{\rho_0} \delta_{i3} - \frac{\partial \tau_{ki}}{\partial x_k} + F_i \quad (1)$$

In that equation, suffixes i, j, k represent numbers of 1–3, x_i are Cartesian coordinates, and (u_1, u_2, u_3) are the velocity components (u, v, w) . The parameter $f_j = (0, 2\Omega \cos(\varphi), 2\Omega \sin(\varphi))$ is the Coriolis parameter with Earth's angular velocity Ω and latitude φ , ρ_0 is the reference density of seawater, $\pi^* = p^* + 2/3\rho_0 e$ is the modified pressure with perturbation pressure p^* and SGS turbulent kinetic energy e , g is the gravitational acceleration parameter, δ_{ij} is Kronecker's delta, and ε_{ijk} is Eddington's epsilon. τ_{ki} is a stress term related to SGS motion, which is obtained from the strain related to GS velocity and the coefficient parameter related to the SGS kinetic energy using a 1.5-order closure after Deardorff (1980). Details are presented in Maronga et al. (2015). We extracted the tidal forcing, F_i , from the ADCP data as discussed in Appendix A.

The potential temperature $\bar{\theta}$ is solved from the following equation.

$$\frac{\partial \bar{\theta}}{\partial t} = -\frac{\partial \bar{u}_j \bar{\theta}}{\partial x_j} - \frac{\partial \bar{u}'_j \bar{\theta}'}{\partial x_j} - \bar{u}_j \frac{\partial \bar{\theta}}{\partial x_j} - \alpha(\langle \bar{\theta} \rangle - \theta(z)) \quad (2)$$

The second term on the right side shows the influence of SGS, which is obtained from the SG equation. The third term shows advection based on the temperature gradient of the basic field $\partial \bar{\theta} / \partial x_j$, which is a function of z only.

The numerical model has no mechanism for maintaining stratification such as radiation heating and surface heat flux. Therefore, the stratification is destroyed by turbulent mixing with time passage of the model. In the long run, without this forcing, the bottom boundary layer width increases with erosion of the stratified region. Therefore, we assumed a restoring source (Newtonian damping) only for the temperature because the temporal variation of temperature is less than that of salinity, which can guarantee the free temporal change of salinity. Direct inclusion of a restoring term in the prognostic equation reduces the temperature anomaly related to turbulent eddy and thereby reduces the turbulence. Therefore, we calculate the horizontal mean temperature $\langle \bar{\theta} \rangle$ in each model time step. Then the additional heating/cooling related to the difference between the horizontal mean model temperature and the reference temperature $\theta(z)$, which is horizontally uniform, is added to the prognostic equation of temperature; the last term in Eq. (2). The horizontal averaged temperature is relaxed to the basic temperature field on the relaxation time scale of $1/\alpha$.

We restore the horizontal mean model temperature to the horizontal uniform reference temperature in this way. The observed vertical temperature gradient is a result realized after the effects from turbulent vertical mixing against the heating source. Therefore, the reference temperature field is expected to have slightly stronger stratification. The reference temperature is the time mean observational temperature, but with addition of the linearly increasing temperature with the gradient 1°C per 100 m as shown by the dashed line in Fig. 2a. The relaxation time for adjustment to the reference temperature field is 2 h. This relaxation effect is not so decisively large because the time change of the model temperature can be recognized, as described later. This value is adopted to represent the observation well. In this sense, this parameter is a tuning parameter for this study.

Salinity \bar{S} is solved from a similar equation as

$$\frac{\partial \bar{S}}{\partial t} = -\frac{\partial \bar{u}_j \bar{S}}{\partial x_j} - \frac{\partial \bar{u}'_j \bar{S}'}{\partial x_j} - \bar{u}_j \frac{\partial \bar{S}}{\partial x_j} \quad (3)$$

The second term on the right side is the contribution from the SGS.

The adjusting term is not included in the salinity equation, which can guarantee the free temporal change of salinity. The last term shows advection based on the salinity gradient of the basic field $\partial \bar{S} / \partial x_j$, which is a function of z only. The temperature and salinity gradients were obtained from the observational value of slightly separated observation points in Fig. 1. The estimated horizontal gradients of temperature and salinity are depicted in Fig. 3.

In addition to the standard experiment reproducing the observation results using these equations, in order to investigate the influence of the horizontal advection effect of temperature and salinity, a sensitivity experiment is carried out by dropping the third terms in Eqs. (2) and (3).

We used the initial conditions of the potential temperature and salinity as the time mean of all observed data, as presented in Fig. 2. The observed salinity profile has an inversion layer at about 25 m depth, which is compensated by the decrease in the potential temperature. Therefore, the stratification is hydrostatically stable. We removed this inversion of salinity by connecting both ends of it smoothly to weaken the shock caused by the initial conditions.

We estimated the initial conditions of velocity from the tidal component of ADCP data. First, the M_2 and K_1 constituent tides were extracted from ADCP velocity data using least squares method. The tidal elliptic was obtained for each constituent. Their four parameters of major and minor axes, the inclination of the major axis, and the initial phase of tidal elliptic can provide the analytical solution and its forcing (Godin, 1972; Wakata, 2013). The concrete method is described in Appendix A. The ADCP observations were started at 16:40 Japan Standard Time (JST) on 16 July 2011. The initial condition of velocity was set to the barotropic analytical solution of tidal equation with constant vertical viscosity of $0.001 \text{ m}^2 \text{ s}^{-1}$ for the M_2 and K_1 constituents on the day before the first ADCP observation by turning back the time of the barotropic analytical solution (A.2) one day for adjustment to the surrounding baroclinic fields. The numerical simulation was conducted for 6 days covering the ADCP observation period.

3. Results

The LES numerical simulation results are presented here for comparison to observation results obtained for the East China Sea (Endoh et al., 2016). The tidal components are also analyzed for the velocity data of both the simulation and observations.

3.1. Scalar fields

Scalar fields such as the observed temperature and salinity (Endoh et al., 2016) are portrayed in Fig. 4. The temperature does not change much on a temporal basis compared to salinity. The thermocline exists from 30 m depth to 8 m. The well-mixed bottom boundary layer exists below 30 m depth. The surface mixed layer exists above 8 m depth (see also Fig. 2a). The salinity is also mixed deeper than 30 m depth, but it changes periodically over time. Low salinity appears to occur at around 18:00 on 17 and 18 July, with a period of about 24 h around 30–40 m depth in the bottom boundary layer, whereas high salinity appears at around 00:00 and 12:00 on 18 and 00:00 on 19 July with the period of 12 h in the lower region. In other words, the salinity changes semidiurnally near the bottom, but diurnally near the middle. The turbulent dissipation rate is portrayed in Fig. 4c, which can express the turbulence activity. A patches of elevated dissipation appears 00:00 on 18 and 19 July around 30–40 m depth, whereas higher areas appear with a period of about 6 h on 17 and 18 July at around 60–65 m depth, but they are somewhat feeble. In other words, the turbulent dissipation rate varies diurnally at around 30–40 m depth and quarter-diurnally near the bottom. Simpson et al. (1996) obtained the M_4 variation of dissipation rate near the bottom of the Irish Sea, as induced by strong vertical shear related to M_2 tidal constituents. This M_2 constituent can pass the major axis twice for passage around the ellipse in the M_2

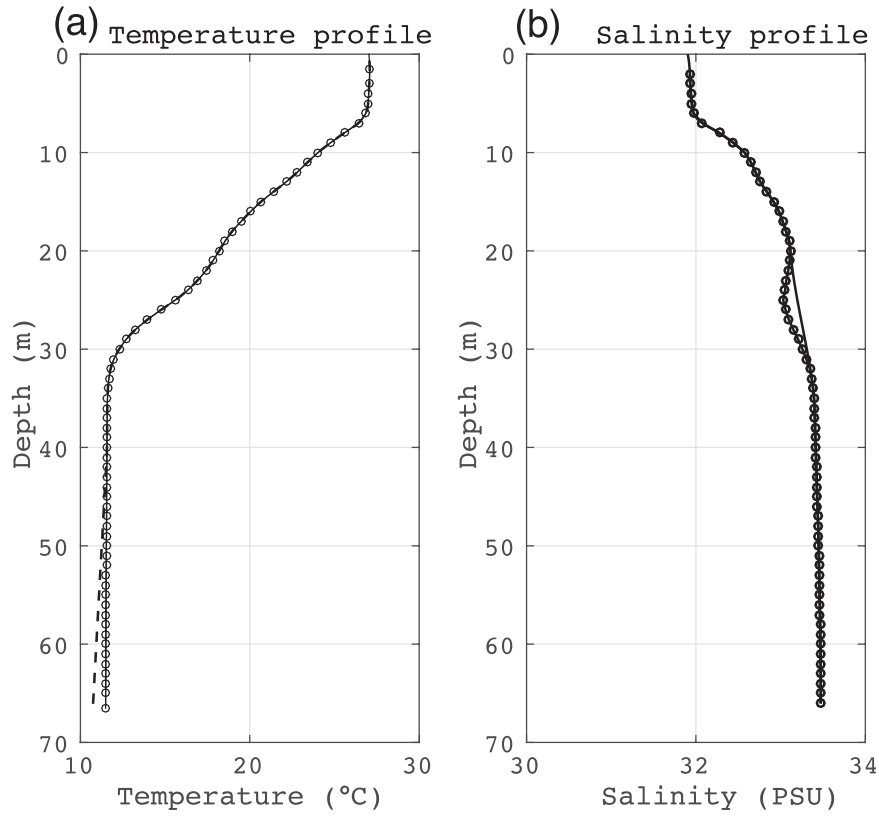


Fig. 2. Vertical profiles of temperature (a) and salinity (b) at the star symbol site in Fig. 1. Smoothed line are time mean at each depth. The dashed line is the relaxation reference temperature considering additional heating.

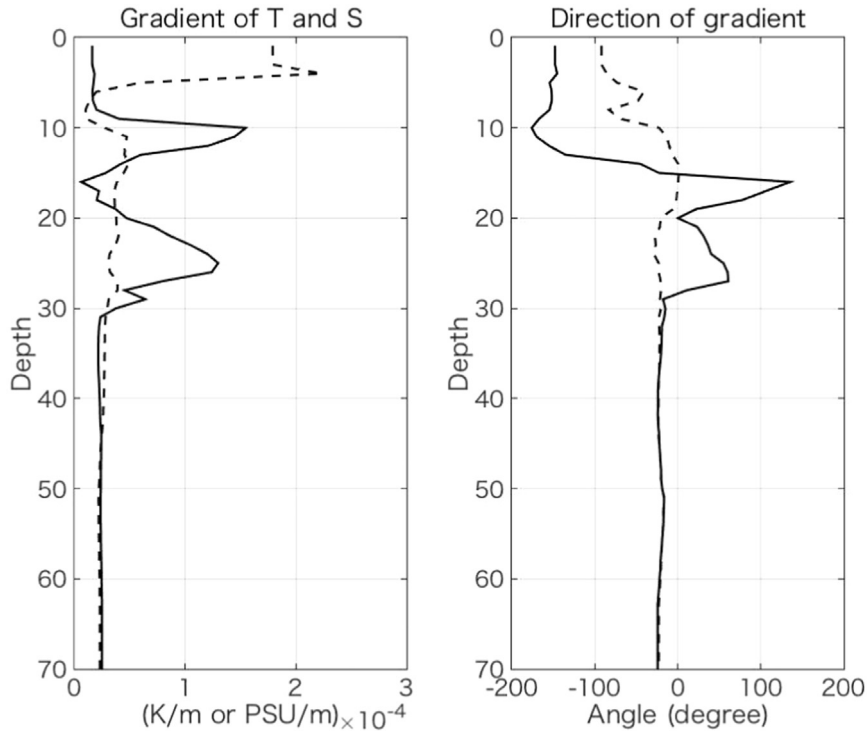


Fig. 3. Horizontal gradient of temperature (solid line) and salinity (dashed line) at left. Their directions are shown, respectively, at right. Zero degrees is eastward.

period. Therefore, the dissipation rate varies with the half period of M_2 i.e. M_4 . The diurnal variation in the upper part of boundary layer in the present observation was not found in observations reported by Simpson et al. The mechanism of this variation is discussed later.

The LES results are presented in Fig. 5, which shows the horizontal

mean value in the numerical domain. The temperature can maintain stratification because of relaxation heating, but feeble diurnal variation caused by horizontal advection is apparent. Therefore, the relaxation effect to the temperature field is not so large as to suppress the time variation of the temperature completely. The salinity evolves similarly

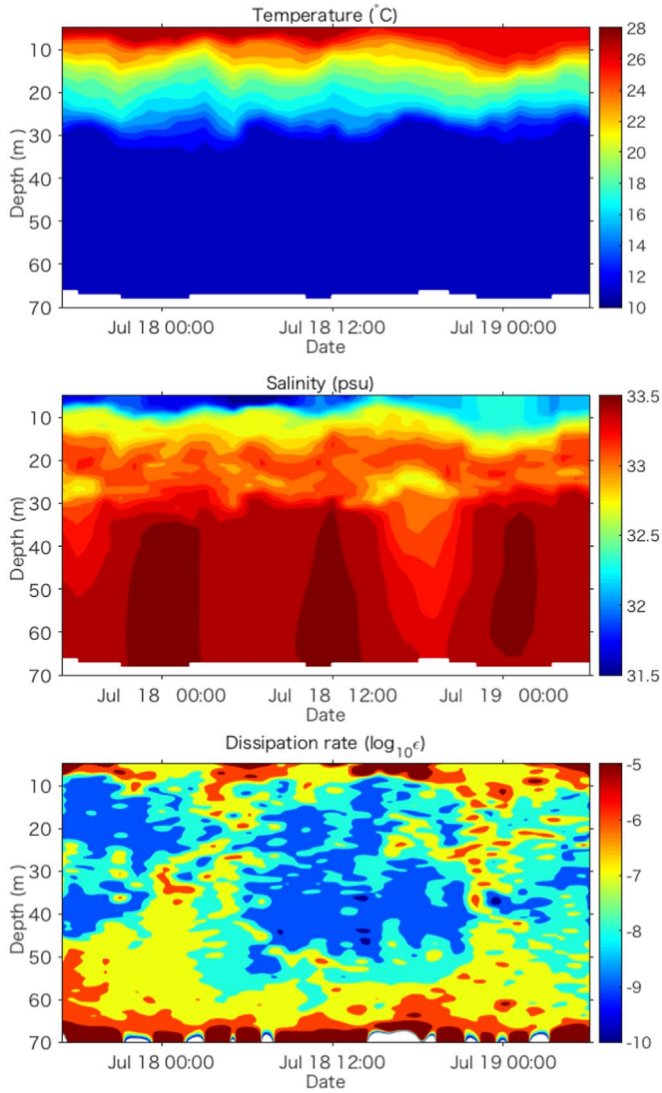


Fig. 4. Time–depth sections of temperature (top), salinity (middle), and logarithm of energy dissipation rate ϵ (W kg^{-1}) (bottom) of observations (Endoh et al., 2016).

to the observation. Predominant diurnal variation exists under the thermocline. The semidiurnal signal exists at a lower depth. The turbulent energy dissipation rate is obtainable from the dissipation rate in the SGS energy equation. Semidiurnal variation exists near the seabed, although, at around 40 m depth, diurnal variation exists in accordance with the observation. The energy dissipation rate shows a relatively small value above 40 m depth, which differs greatly from the observation. The mean dissipation rate, depicted in Fig. 6, shows good agreement with observations under the thermocline except in the immediate vicinity of the seabed, but it decreases rapidly above the thermocline. This decrease above the thermocline has been reported from other studies (Simpson et al., 1996; Werner et al., 2003) that have used ensemble closure models. Similar trend is seen in the LES.

3.2. Current fields

We plot the velocity field from the ADCP in Fig. 7. The semidiurnal tide M_2 is outstanding, but their peak values of velocity and their vertical extent is varied in each phase. For instance, the east–west velocity is strong, with a peak located at around 40 m depth on the latter half of the 17, although it is weak, with a peak located at around 50 m depth on the first half of the 18. These differences might be understood from the overlapping of M_2 and K_1 tidal constituents, as

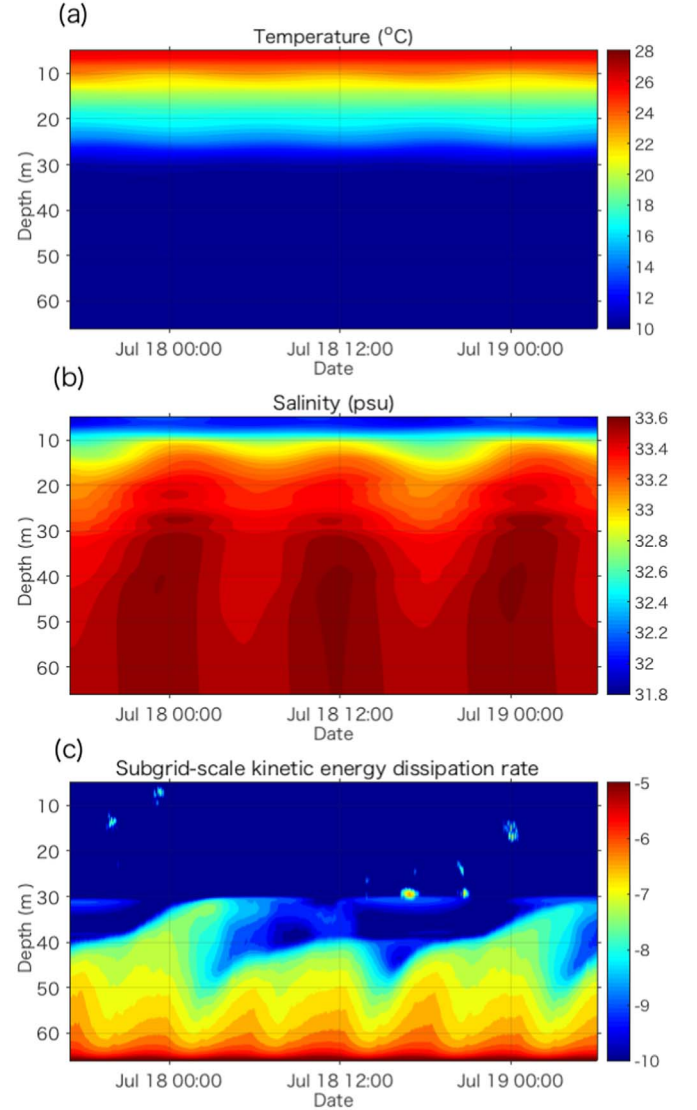


Fig. 5. Same as Fig. 4, but LES model results.

discussed later. Fig. 8 shows the time–height section of east–west currents u and north–south currents v from the LES study. The simulation results can capture the main properties of current observations such as the peak position and the modulation of amplitude, but the magnitude is somewhat weak near the seabed. The LES current can well capture the ADCP current features.

After extracting the M_2 and K_1 tidal components from the current data using least squares method, we regard these modes as representing signals with approximately semidiurnal and diurnal periods including close tidal periods components such as S_2 and O_1 , rather than their exact period signal, because the observation period of about 5 days is not long enough to separate more modes. The analyzed results of ADCP observation are depicted in Fig. 9. The LES results are presented in Fig. 10. In the ADCP observation, the M_2 amplitude decreases gradually with depth downward below 55 m depth. The reduced depth scale of M_2 , which indicates the bottom boundary layer thickness related to M_2 , is about 10 m, whereas the amplitude of K_1 decreases under 30 m depth. The boundary layer thickness is about 35 m. The vertical amplitude profiles of M_2 and K_1 modes differ greatly. For that reason, the latitude of observations is quite close to the critical latitude of K_1 (30°N), where Coriolis parameter f equals the angular frequency ω of the K_1 tide. Then, the bottom boundary layer becomes extremely thick because its depth is proportional to $\sqrt{\nu/|f - \omega|}$ for the

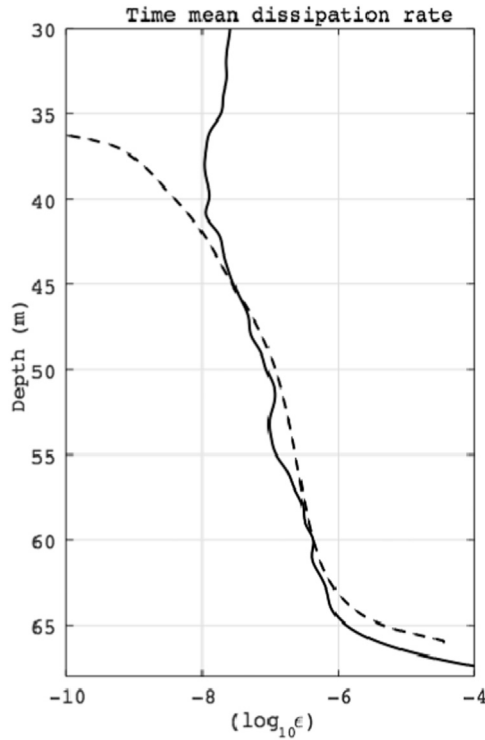


Fig. 6. Time mean logarithmic dissipation rate ε (W kg^{-1}) of the observations (solid line) and LES (dashed line).

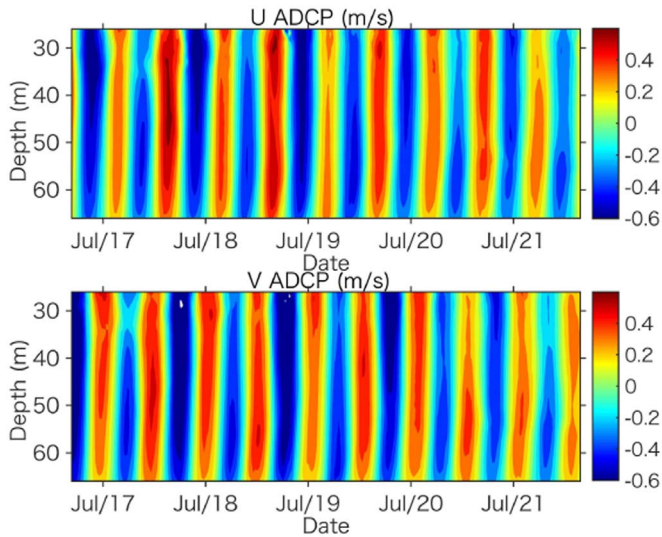


Fig. 7. Time–depth section of east–west velocity (top) and north–south (bottom) for the ADCP observation.

case of constant vertical eddy viscosity ν (ref. Eq. (A-2) in Appendix A).

Orientation of the major axis of tidal ellipsoid is not changed with depth if the latitude of the observed location is higher than the critical latitude (30°N for K_1 and 74.5°N for M_2), although it rotates counterclockwise $\pi/4$ toward the sea bottom if the latitude is lower, as discussed by Wakata (2013). That study estimated the rotation of ellipsoid axis from the seabed limit asymptotic form of analytical solution. The orientation of the M_2 major axis is not so different (Fig. 9b) because the observation site is far south from the critical latitude of M_2 , whereas that of K_1 rotates counterclockwise close to $\pi/4$ downward through the boundary because it is slightly northern than the critical latitude of K_1 . This result is consistent with the analytical speculation presented by Wakata (2013). Next, regarding the counterpart of LES study, the boundary layer width of M_2 is thinner than K_1 ,

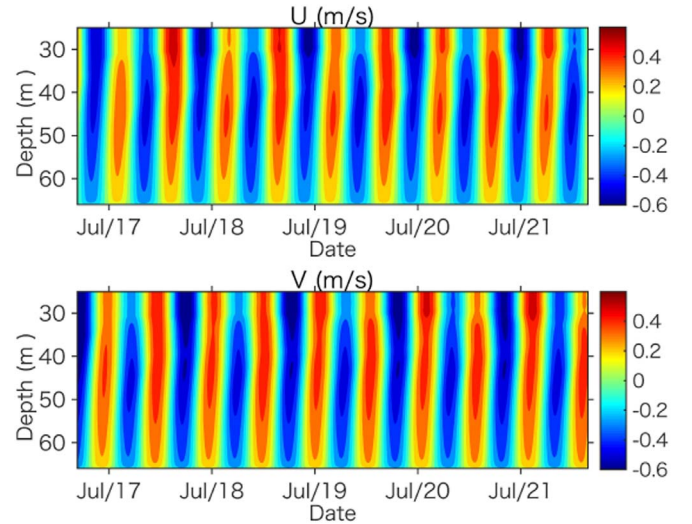


Fig. 8. Same as Fig. 7, but LES model results.

similar to the observation results, but they are slightly thicker than the observation. The K_1 amplitude decreases rapidly from 30 m depth to 45 m depth, which is the top of the M_2 boundary layer, but it is small in the M_2 boundary layer. This feature is also recognized to a slight degree in the observation results. This vertical profile of K_1 is quite peculiar and interesting. The spatial and temporal variation of the vertical eddy viscosity might be candidates for this reason. We speculate that the temporal variation of the eddy viscosity, which is large in the M_2 boundary layer, might induce the inertial oscillation there. The amplitude of this inertial oscillation is added to the amplitude of K_1 constituent and the K_1 amplitude is contaminated because the period of inertial oscillation is close to that of K_1 . Nevertheless, this cannot be clarified now. There is a possibility of the numerical artifacts for the sharp gradient of temperature around the thermocline. The orientation of the major axis of M_2 tidal ellipsoid is not changed downward, but K_1 is varied almost 45° , as in the observations and linear solution of tidal equation.

4. Mechanism underlying diurnal variation of the dissipation rate

We next consider the mechanism of temporal variation of the dissipation rate, which shows diurnal variation in the upper part of the boundary layer but quarter-diurnal M_4 variation in the lower part. The quarter-diurnal M_4 variation can be explained simply from twice passage of the major axis of the tidal ellipsis, where the current is maximum, in the one rotation around M_2 tidal ellipsis. However, it is quite curious why the diurnal variation in the upper part appears because it cannot be explained from the rotation in the K_1 tidal ellipsis, i.e., it only derives a half-day variation.

Regarding the temporal change of salinity, it varies diurnally at the middle depth, which might alter the stratification and stability. The subsequent stratification change might suppress or enhance turbulence. This is a possible hypothesis to explain the diurnal variation of the dissipation rate. This mechanism controlling turbulence is analogous to strain-induced periodic stratification observed in “regions of freshwater influence (ROFI)” such as the Rhine region (the North Sea) and Liverpool Bay (Simpson et al., 1990; Simpson and Souza, 1995). In the ROFI region, a horizontal salinity (i.e. density) gradient prevails because of diluted water spreading from the river. The diluted water covers above the bottom higher salinity water on the ebb phase of the tide. Then turbulence is suppressed by strong stratification, whereas the flood phase the offshore high salinity water covers above the lower salinity bottom water. The weak stratification enhances the turbulence.

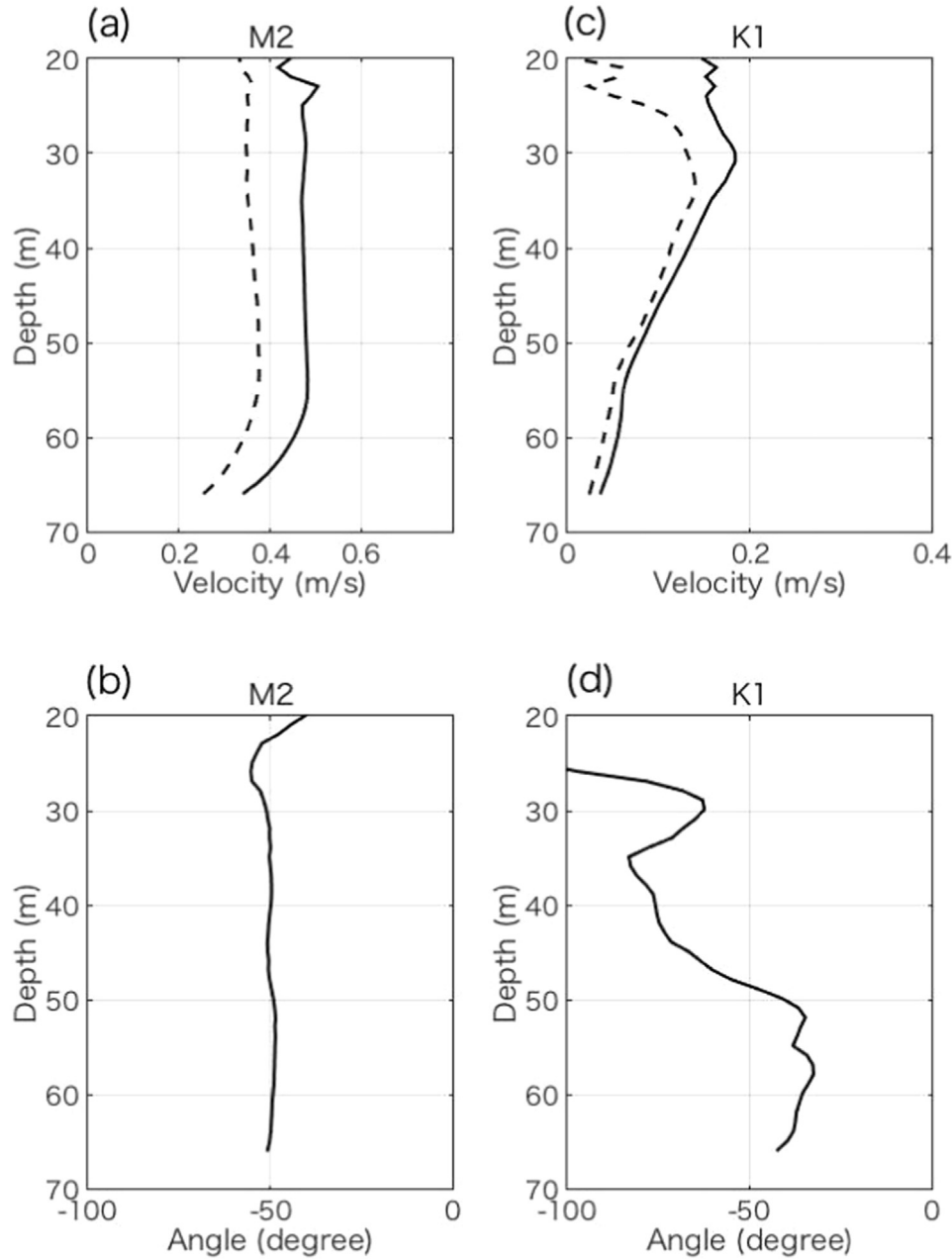


Fig. 9. Major (solid) and minor (dashed) axes of observed tidal ellipses for semidiurnal tide constituent (a) and diurnal (c). Orientation of major axis of observed tidal ellipses for semidiurnal (b) and diurnal (d). Zero degrees is eastward.

These processes are caused by the difference between the bottom and middle current speeds (i.e. strain). The strain-induced stability control and the bottom stirring by the tidal flow can produce successive oscillation of the turbulent intensity.

Although the present observation point is about 400 km east-northeast from the Changjiang River mouth, the salinity oscillates to a striking degree because of the horizontal advection of salinity. It remains unclear whether the horizontal gradient of salinity derives from the discharged flow directly or by the vertical mixing of the discharged surface diluted water depending on the bathymetry. Leaving aside this question, we conducted a hypothetical experiment without horizontal advection to confirm whether the strain-induced stability control mechanism occurs in the East China Sea.

We run the model excluding the horizontal advection term related to the large scale gradient of salinity and temperature i.e. the third terms in Eqs. (2) and (3). Fig. 11 is the dissipation rate for the non-

advection case, which closely resembles the case with advection in Fig. 5(c). The typical value of horizontal density gradient for the Rhine ROFI is about $2.5 \text{ kg m}^{-3} \text{ km}^{-1}$ (Simpson et al., 1995), but the horizontal density gradient is about $1.5 \times 10^{-2} \text{ kg m}^{-3} \text{ km}^{-1}$ for the present case. It is smaller by two orders of magnitude (Endoh et al., 2016). Although the salinity oscillates diurnally, we infer that the strain-induced periodic stratification control mechanism observed in ROFI is not a direct cause of diurnal variation of the dissipation rate in the upper part of the boundary layer. This variation cannot be explained from the suppression (sink) side through stratification controlled by the tidal current strain. Therefore, we will consider it from the forcing (source) side. We estimate the turbulence source term as $-\langle \mu' w' \rangle \frac{d\bar{u}}{dz} - \langle v' w' \rangle \frac{d\bar{v}}{dz}$, where $\langle u'v' \rangle$ and $\langle v'w' \rangle$ are the grid-scale Reynolds stress, and where $d\bar{u}/dz$ and $d\bar{v}/dz$ represent the vertical shear of horizontal mean velocity (Fig. 12a). Results show that the diurnal signal for the forcing exists at around 40 m depth, which has a pattern

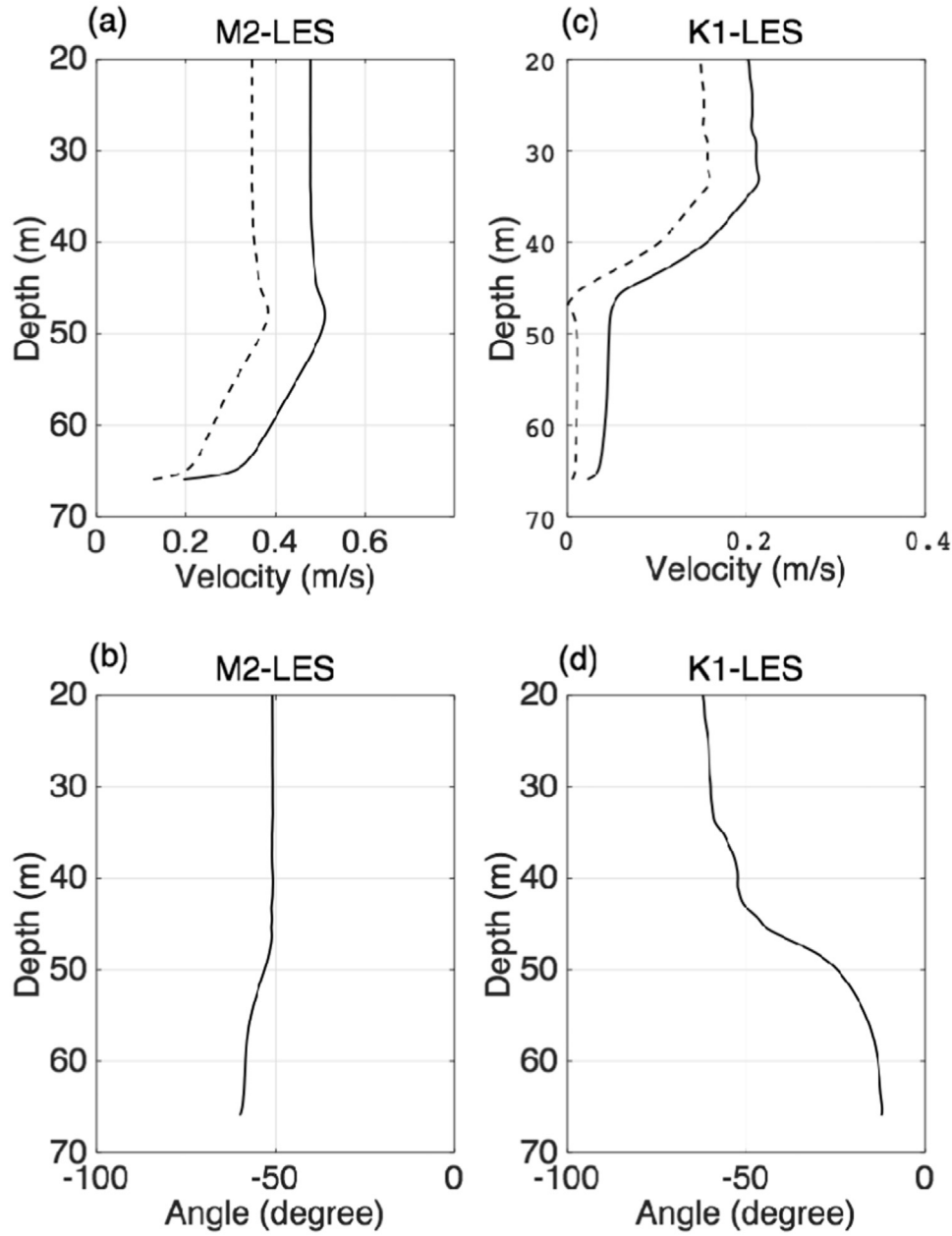


Fig. 10. Same as Fig. 9, but LES model results.

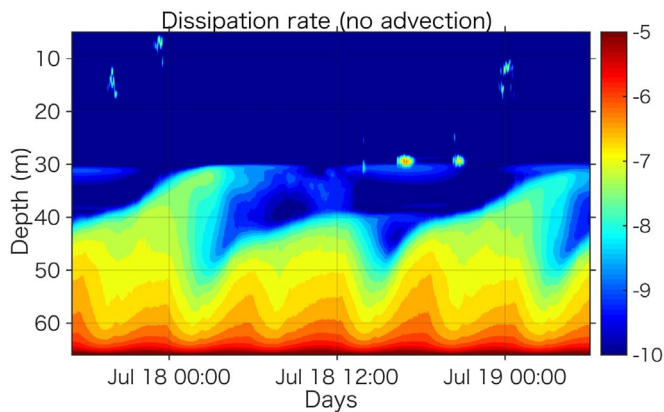


Fig. 11. Time–depth section of logarithmic energy dissipation rate ε (W kg^{-1}) from LES model simulation, excluding the horizontal advection of temperature and salinity.

resembling that of the diurnal signal of the dissipation rate. This source term is the product of Reynolds stress and vertical shear. The diurnal signal of Reynolds stress (not shown) is not so large, but the vertical shear ($\sqrt{(d\bar{u}/dz)^2 + (d\bar{v}/dz)^2}$) has a large diurnal signal superposed with a semidiurnal signal presented in Fig. 12(b). K_1 has a thicker boundary layer than M_2 . The major axis of tide ellipse rotates counterclockwise downward because the observation point is close to the critical latitude associated with K_1 , as discussed before. This thick boundary layer can induce diurnal variation of the vertical shear around the upper part of the boundary layer. The vertical shear peak is expected to appear two times a day when the current directs the major axis of tidal ellipses twice for one rotation if we only consider the vertical shear of K_1 . However, M_2 also has small vertical shear because of the vertical time-phase difference of rotation. M_2 , with a half-day period, and K_1 , with its one day period, can direct the same direction once a day, i.e. interference. These constituents can evoke interference with the diurnal period. The present LES study suggests the conclusion that the mechanical production rate related to the interference is the cause

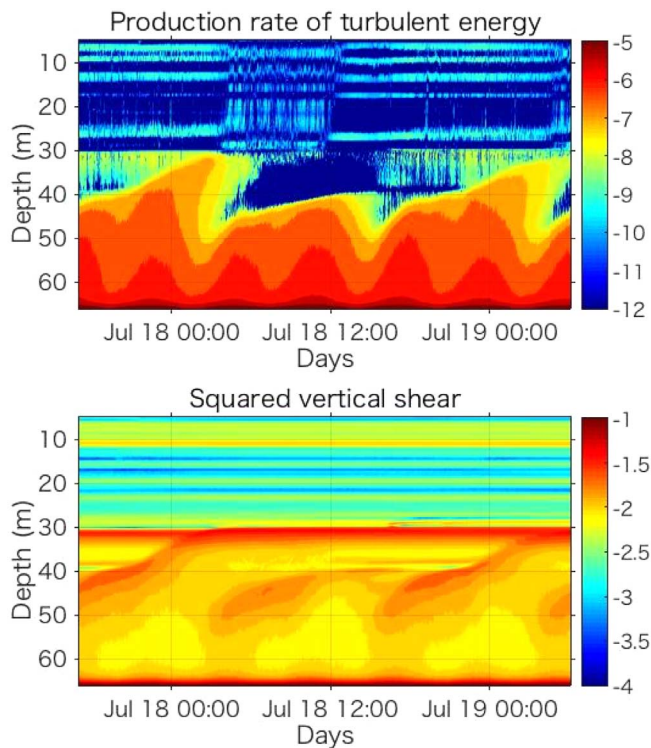


Fig. 12. (a) Production rate of turbulent energy ($\text{m}^2 \text{s}^{-3}$) and (b) squared vertical shear of horizontal mean currents ($\text{m}^2 \text{s}^{-2}$).

for diurnal variation of the dissipation rate in the upper part of the bottom boundary layer of the East China Sea rather than the suppression or enhancement effect related to the strain-induced periodic stratification control which usually occurs in ROFI regions.

5. Summary and discussion

Turbulence originating from the tidal current near the seabed in the East China Sea was studied using LES model simulation. Comparison between observations and LES model simulation results was conducted to clarify the mechanism of the temporal variation of the turbulent energy dissipation rate. The study of turbulence near the seabed is, in a sense, an ideal condition for the present purposes because the abyssal forcing of turbulence is not so complicated as that near the surface region, which includes many uncertain effects such as the wind waves, Langmuir circulation, surface momentum, and heat flux (Skylingstad et al., 1999). These effects might be obstructed by strong stratification around the thermocline. The subsequent periodic variation is found under the thermocline compared with intricate variation near the surface region.

The model can substantially capture the primary trend of the observations. We regard the LES model as a useful tool for studying ocean turbulence. The LES model can readily afford the many physical parameters that are usually difficult to obtain from observations. Hypothetical experiments as changing the background state or forcing can be helpful to clarify the mechanism. We conducted two experiments with/without horizontal advection to elucidate the diurnal variation of the dissipation rate in the upper part of the bottom boundary layer in the East China Sea, for which we found that interference of M_2 and K_1 constituents is important. The interference

of multiple constituents can change the turbulence activity through their shear production. The latitude of the observation site ($31^\circ 44.9' \text{N}$) is close to the critical latitude of K_1 (30°N). Therefore, multiple constituents with different vertical structures are present. The temporal behavior of the dissipation rate was more complex than the result for the Irish Sea (around 54°N) reported by Simpson et al. (1996), for which only the effect of M_2 on turbulent energy dissipation rate was found to be dominant. Furevik and Fodvik (1996) reported high nutrients around the M_2 critical latitude 74.5°N in the Barents Sea. They emphasized the relation of vertical mixing and the critical latitude.

Endoh et al. (2016) discussed the importance of upslope and downslope flow effects in the lower part of bottom boundary, which change the stratification and which engender unstable stratification during upslope flow because the upslope flow conveys the deeper dense water on top of less dense water that moves slowly because of friction. When the salinity peak appears, a region in which the buoyancy frequency has a small negative value appears below 30 m depth (Fig. 2 in Endoh et al. (2016); shown by blank area). Increase of dissipation rate in response to unstable stratification is apparently unclear, which is consistent with the results of numerical simulations (Umlauf and Burchard, 2011). However, Lorke et al. (2008) noted that even though this effect accounts for only a small contribution to turbulence production, the contribution to the diffusivities is important because of the large mixing length scale during unstable stratification. The increased diffusivities during the unstable stratification mix up sediment, which is transported upslope by several mechanisms as tidal pumping or tidal strain. The present model is assumed to have a flat bottom. Therefore, we cannot investigate this effect. This process would occur quite near the seabed. We discussed only the upper part of the boundary layer in the present research. The bottom slope effect will be left as a subject for later research.

The present simulation has a weak dissipation rate above and around the thermocline. Several researchers have noted this dissipation rate weakness. We speculate that a possible reason is the small scale of turbulent eddies because of the strong vertical stratification, which may weaken the LES capabilities as discussed by Basu and Porte-Agel (2006) and Beare and Coauthors (2006). The other reason is the lack of surface forcing; a lack of background turbulence. The similar results are also obtained in ensemble closure model studies (Simpson et al., 1996; Burchard et al., 1998). Burchard et al. (1998) introduced the use of an artificial minimum value for vertical eddy viscosity and thereby avoided this problem. It might be necessary to include background turbulent forcing for the present type of LES study. The LES model fundamentally succeeds in simulating the observation results. We hope that the present research can become an instructive first step in the use of LES to simulate actual ocean phenomena.

Acknowledgments

This work was supported by JSPS KAKENHI Grant no. JP22340140, and from the Collaborative Research Program of Research Institute for Applied Mechanics (RIAM), Kyushu University. Dr. S. Raasch is appreciated for helping in the use of PALM and for valuable discussions. We thank the anonymous reviewers for careful reading of our manuscript and their constructive comments and suggestions. Computations were conducted mainly using the computer facilities at Research Institute for Information Technology, Kyushu University.

Appendix A. Linear tidal solutions and estimation for tidal forcing

The linear tidal solution in the planetary boundary layer is obtained as a solution for the following equation (Soulsby, 1983; Maas and van Haren, 1987)

$$\frac{\partial \omega}{\partial t} + i f \omega - \nu \frac{\partial^2 \omega}{\partial z^2} = F \quad (\text{A.1})$$

where ω is the complex function of $u + iv$, and ν is the eddy viscosity, and $F (F_x + iF_y)$ is tidal forcing term. The solution of this equation was noted in Wakata (2013). Here, we summarize how to estimate the external force and corresponding solution from the current data. The hodograph of the tidal current can be denoted by an ellipse, and the ellipse can be expressed by superimposing the clockwise circular locus and the counterclockwise circular locus in the (u, v) plane. The solution of (A.1) was demonstrated in many studies, but they are only a special case and the corresponding forcing term is not stated. Wakata (2013) noted the solution and forcing term as a general form. If we assume ν is constant and the boundary condition $\omega = 0$ at the seabed and at z infinity (the origin of z is at the seabed and upward is positive), then the solution is shown below.

$$\begin{aligned} \omega = & \frac{(U_{maj} + U_{min})}{2} \left[1 - \exp\left(-\sqrt{\frac{s_p(f + \sigma)}{2\nu}} (1 + i s_p) z\right) \right] \exp(i\sigma t + i\phi + i\Gamma) \\ & + \frac{(U_{maj} - U_{min})}{2} \left[1 - \exp\left(-\sqrt{\frac{s_m(f - \sigma)}{2\nu}} (1 + i s_m) z\right) \right] \exp(-i\sigma t - i\phi + i\Gamma) \end{aligned} \quad (\text{A.2})$$

The corresponding forcing term F is

$$\begin{aligned} F = & i(f + \sigma) \frac{U_{maj} + U_{min}}{2} \exp(i\sigma t + i\phi + i\Gamma) \\ & + i(f - \sigma) \frac{U_{maj} - U_{min}}{2} \exp(-i\sigma t - i\phi + i\Gamma), \end{aligned} \quad (\text{A.3})$$

where $s_p = \text{sign}(f + \sigma)$ and $s_m = \text{sign}(f - \sigma)$ ($\text{sign}(x)$ is 1 if x is positive and -1 if negative). U_{maj} is major axis of tidal ellipse, U_{min} is minor axis outside the boundary layer. σ is the angular frequency, which is defined as positive/negative if the hodograph rotates counterclockwise/clockwise. Γ is the angle of major axis and ϕ is the initial phase. This ϕ is not the initial orientation of velocity vector Ψ in the tidal ellipse (Fig. A.1).

The parameters included in the solutions are obtained by comparing the solution assumed ν being zero (i.e. the second terms in the bracket is zero) with the time series of the observed currents outside the boundary layer. This study examines the M_2 and K_1 constituents. Therefore, we compare the current data and the harmonic components with M_2 and K_1 frequency only (i.e. σ_M and σ_K respectively) to find their amplitude and phase Fig. A.2.

$$\begin{aligned} \Phi_u = & (u(t) - (u_0 + u_{CM} \cos(\sigma_M) + u_{SM} \sin(\sigma_M) + u_{CK} \cos(\sigma_K) + u_{SK} \sin(\sigma_K)))^2 \\ \Phi_v = & (v(t) - (v_0 + v_{CM} \cos(\sigma_M) + v_{SM} \sin(\sigma_M) + v_{CK} \cos(\sigma_K) + v_{SK} \sin(\sigma_K)))^2 \end{aligned} \quad (\text{A.4})$$

The coefficient is determined using the method of least squares so that Φ is minimized. We introduce the following parameters for M_2 constituents.

$$\begin{aligned} R_P = & 0.5 \sqrt{((u_{CM} + v_{SM})^2 + (u_{SM} - v_{CM})^2)} \\ R_M = & 0.5 \sqrt{((u_{CM} - v_{SM})^2 + (u_{SM} + v_{CM})^2)} \end{aligned} \quad (\text{A.5})$$

Then, the major and minor axes are determined as shown below.

$$\begin{aligned} U_{maj} = & R_P + R_M \\ U_{min} = & (R_P - R_M) \text{sign}(R_P - R_M) \end{aligned} \quad (\text{A.6})$$

If $\text{sign}(R_P - R_M)$ is positive/negative, then it rotates counterclockwise/clockwise. Therefore, $\sigma = \text{sign}(\phi_P - \phi_M) \sigma_M$. We introduce the following parameters as

$$\begin{aligned} \phi_P = & \text{atan}(-(u_{SM} - v_{CM})/(u_{CM} + v_{SM})) \\ \phi_M = & \text{atan}((u_{SM} + v_{CM})/(u_{CM} - v_{SM})) \end{aligned} \quad (\text{A.7})$$

Then the tilt angle of ellipse and the initial phase are the following.

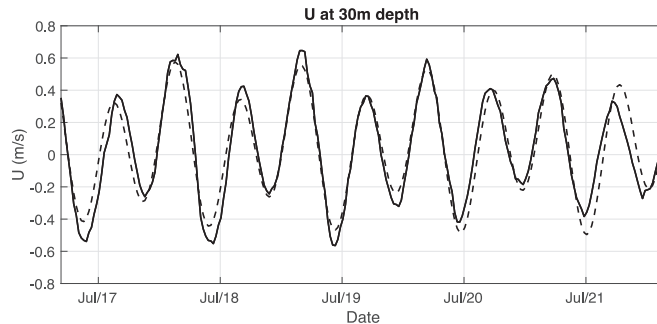


Fig. A1. East–west velocity at 30 m depth. The solid line shows the ADCP current observation. The broken line shows the velocity reconstructed from K_1 and M_2 constituents extracted from the observed current data.

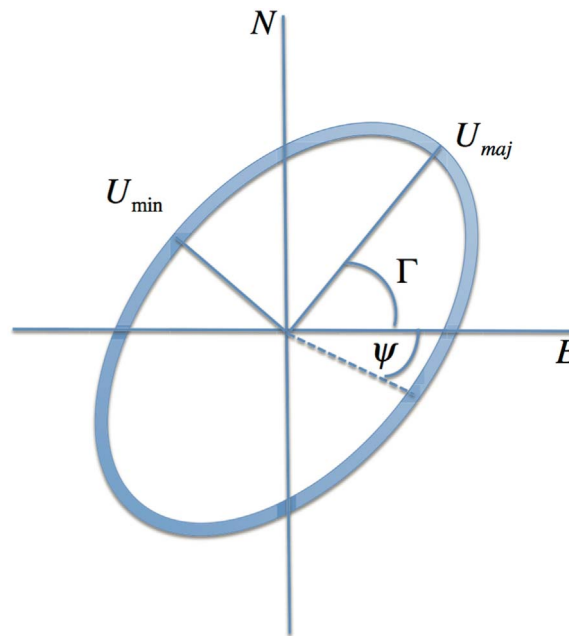


Fig. A2. Tidal hodograph: U_{maj} (U_{min}) represents the velocity of major (minor) axis direction; Γ is the direction angle of the major axis; and ψ is the initial angle. The positive x-axis

$$\Gamma = 0.5(\phi_P + \phi_M)$$

$$\phi = 0.5(\phi_P - \phi_M)\text{sign}(\phi_P - \phi_M)$$

(A.8)

Tidal solutions and forced functions are obtainable from these parameters. When multiple constituents exist, because linearity is established, the solutions and forced functions are obtained as the sum of separately obtained ones.

References

- Basu, S., Porte-Agel, F., Fofoula-Georgiou, E., 2004. Development of stable boundary layer parameterizations in numerical weather prediction models: a scale-dependent dynamic LES modeling approach. In: *Proceedings of the 16th Symposium on Boundary Layers and Turbulence*, pp. 699–702.
- Basu, S., Porte-Agel, F., 2006. Large-eddy simulation of stably stratified atmospheric boundary layer turbulence: a scale-dependent dynamic modeling approach. *J. Atmos. Sci.* 63, 2074–2091.
- Beare, R.J., Coauthors, 2006. An intercomparison of large-eddy simulations of the stable boundary layer. *Bound-Lay. Meteorol.* 118, 247–272.
- Burchard, H., Petersen, O., Rippeth, T.P., 1998. Comparing the performance of the Mellor–Yamada and the k- ϵ two-equation turbulence models. *J. Geophys. Res.* 103, 10543–10554.
- Deardorff, J.W., 1980. Stratocumulus-capped mixed layers derived from a three-dimensional model. *Bound. Layer. Meteorol.* 18 (4), 495–527.
- Endoh, T., Yoshikawa, Y., Matsuno, T., Wakata, Y., Lee, K.-J., Umlauf, L., 2016. Observational evidence for tidal straining over a sloping continental shelf. *Cont. Shelf Res.* 117, 12–19.
- Furevik, T., Foldvik, A., 1996. Stability at M_2 critical latitude in the Barents Sea. *J. Geophys. Res.* 101, 8823–8837.
- Gayen, B., Sarkar, S., Taylor, J.R., 2010. Large eddy simulation of a stratified boundary layer under an oscillatory current. *J. Fluid Mech.*, 643. <http://dx.doi.org/10.1017/S002211200999200X>.
- Godin, G., 1972. *The Analysis of Tides*. Liverpool University Press, 264, (Chapter 2).
- Li, M., Garrett, C., Skillingstad, E., 2005. A regime diagram for classifying turbulent large eddies in the upper ocean. *Deep-Sea Res. I* 52 (2), 259–278.
- Li, M., Radhakrishnan, S., Piomelli, U., Geyer, W.R., 2010. Large-eddy simulation of the tidal-cycle variations of an estuarine boundary layer. *J. Geophys. Res.* 115, C08003. <http://dx.doi.org/10.1029/2009JC005702>.
- Li, M., Trowbridge, J., Geyer, R., 2008. Asymmetric tidal mixing due to the horizontal density gradient. *J. Phys. Oceanogr.* 38, 418–434.
- Lorke, A., Peeters, F., Wuest, A., 2005. Shear-induced convective mixing in bottom boundary layers on slopes. *Limnol. Oceanogr.* 50 (5), 1612–1619.
- Lorke, A., Umlauf, L., Mohrholz, V., 2008. Stratification and mixing on sloping boundaries. *Geophys. Res. Lett.* 35 (14). <http://dx.doi.org/10.1029/2008gl034607>.
- Lu, Y.Y., Lueck, R.G., Huang, D.Y., 2000. Turbulence characteristics in a tidal channel. *J. Phys. Oceanogr.* 30 (5), 855–867.
- Lueck, R.G., Lu, Y., 1997. The logarithmic layer in a tidal channel. *Cont. Shelf Res.* 17, 1785–1801.
- Maas, L.R.M., van Haren, J.J.M., 1987. Observations on the vertical structure of tidal and inertial currents in the central North Sea. *J. Marine Res.* 45, 293–318.
- Maronga, B., Gryscha, M., Heinze, R., Hoffmann, F., Kanani-Sühring, F., Keck, M., et al., 2015. The Parallelized large-eddy simulation model (palm) ver. 4.0 for atmospheric and oceanic flows: model formulation, recent developments, and future perspectives. *Geosci. Model. Dev. Discuss.* 8, 1539–1637.
- McWilliams, J.C., Sullivan, P.P., Moeng, C.H., 1997. Langmuir turbulence in the ocean. *J. Fluid Mech.* 334, 1–30.
- Mellor, G.L., Yamada, T., 1974. A hierarchy of turbulence closure models for planetary boundary layers. *J. Atmos. Sci.* 31, 1791–1806.
- Mellor, G.L., Yamada, T., 1982. Development of a turbulence closure model for geophysical fluid problem. *Rev. Geophys. Space Phys.* 20, 851–875.
- Metals, O., 1998. Large-eddy simulations of three-dimensional turbulent flows. *Geophys. Appl. NATO Adv. Sci. I C-Mat.* 516, 351–572.
- Momen, M., Bou-Zeid, E., 2016. Large-eddy simulations and damped-oscillator models of the unsteady Ekman boundary layer. *J. Atmos. Sci.* 73 (1), 25–40.
- Raasch, S., Schröter, M., 2001. PALM – a large-eddy simulation model performing on massively parallel computers. *Meteorol. Z.* 10 (5), 363–373.
- Salon, S., Armenio, V., Crise, A., 2007. A numerical investigation of the Stokes boundary layer in the turbulent regime. *J. Fluid Mech.* 570, 253–296.
- Simpson, J.H., Brown, J., Matthews, J., Allen, G., 1990. Tidal Straining, Density Currents, and Stirring in the Control of Estuarine Stratification. *Estuaries* 13, 125–132.
- Simpson, J.H., Crawford, W.R., Rippeth, T.P., Campbell, A.R., 1996. The vertical structure of turbulent dissipation in shelf seas. *J. Phys. Oceanogr.* 26, 1579–1590.
- Simpson, J.H., Souza, A.J., 1995. Semidiurnal switching of stratification in the region of fresh-water influence of the Rhine. *J. Geophys. Res.* 100 (C4), 7037–7044.
- Skyllingstad, E.D., Smyth, W.D., Moum, J.N., Wuestekera, H., 1999. Upper-ocean turbulence during a westerly wind burst: a comparison of large-eddy simulation results and microstructure measurements. *J. Phys. Oceanogr.* 29, 5–28.
- Soulsby, R.L., 1983. *The Bottom Boundary Layer of Shelf Seas*. Pys. Oceano. Coast. Shelf Seas 35, 189–226.
- Thomas, H., Bozec, Y., Elkalay, K., de Baar, H.J.W., 2004. Enhanced open ocean storage of CO₂ from shelf sea pumping. *Science* 304 (5673), 1005–1008.
- Umlauf, L., Burchard, H., 2011. Diapycnal transport and mixing efficiency in stratified boundary layers near sloping topography. *J. Phys. Oceanogr.* 41 (2), 329–345.
- Wakata, Y., 2010. Numerical simulation of ocean bottom boundary layer. *Theor. Appl. Mech. Jpn.* 58, 145–151.
- Wakata, Y., 2011. Dependence of seafloor boundary layer thickness on the overlying flow direction: a large eddy simulation study. *J. Oceanogr.* 67 (5), 667–673.
- Wakata, Y., 2013. Some properties of tidal currents estimated from analytical and LES simulation studies. *J. Oceanogr.* 69, 737–751.
- Werner, S.R., Beardsley, R.C., Lentz, S.J., Hebert, D.L., Oakey, N.S., 2003. Observations and modeling of the tidal bottom boundary layer on the southern flank of Georges Bank. *J. Geophys. Res.* 108 (C11). <http://dx.doi.org/10.1029/2001JC001271>.